RSC Advances

PAPER

Cite this: *RSC Adv.*, 2024, **14**, 10390

Simultaneously improving the pore structure and electron conductive network of the anode catalyst layer *via* SnO_2 doping for proton exchange membrane water electrolysis

Bang Li,[a] Guangfu Li,[*b] Qiqi Wan,[a] Lei Yuan,[a] Yingying Liu,[a] Longxu Li,[a] Xiaodong Zhuang,[c] Junliang Zhang[a] and Changchun Ke[*a]

Proton exchange membrane water electrolysis (PEMWE) is a promising technology for green hydrogen production. However, its large-scale commercial application is limited by its high precious metal loading, because low catalyst loading leads to reduced electron transport channels and decreased water transportation, *etc.* Herein, we study the electrode level strategy for reducing Ir loading by the optimization of the micro-structure of the anode catalyst layer *via* SnO_2 doping. The pore structure and electron conductive network of the anode catalyst layer can be simultaneously improved by SnO_2 doping, under appropriate conditions. Therefore, mass transfer polarization and ohmic polarization of the single cell are reduced. Moreover, the enhanced pore structure and improved electron conduction network collectively contribute to a decreased occurrence of charge transfer polarization. By this strategy, the performance of the single cell with the Ir loading of 1.5 mg cm^{-2} approaches the single cell with the higher Ir loading of 2.0 mg cm^{-2}, which means that SnO_2 doping saves about 25% loading of Ir. This paper provides a perspective at the electrode level to reduce the precious metal loading of the anode in PEMWE.

Received 11th January 2024
Accepted 24th March 2024

DOI: 10.1039/d4ra00270a

rsc.li/rsc-advances

1. Introduction

Proton exchange membrane water electrolysis (PEMWE), which can produce high-purity hydrogen[1] with high energy conversion efficiency, high current density,[2] and minimal gas permeation between the anode and cathode, is considered a promising technology for large-scale green hydrogen production.[3] In recent years, companies such as Air Liquide, Linde, Elogen, Nel ASA, Ørste, Amprion, and Open Grid Europe have proposed large-scale PEMWE projects.[4]

However, the high cost of the PEMWE stack seriously hinders the widespread application and commercialization of this technology. The utilization of high-loading of platinum group metals, such as platinum (Pt), iridium (Ir), and ruthenium (Ru),[5] in the anode catalyst layer for PEMWE is an important adverse factor to its high cost. In a common 1 MW PEMWE system, approximately 1 to 2 kg Ir is required, while the annual global production of Ir is only about 7000 to 8000 kg.[6]

According to Spori *et al.*,[7] for large-scale applications of PEMWE, the Ir loading should be below 0.05 mg cm^{-2} and less than 0.01 g kW^{-1}. Nevertheless, the current Ir loading in the anode catalyst layer of PEMWE systems is approximately 2 mg cm^{-2},[8] much higher than the target of 0.05 mg cm^{-2}.[9–12] In a word, overcoming the excessively high anode Ir or precious metal loading is crucial for the large-scale commercial application of PEMWE.

Generally, low catalyst loading leads to various challenges, including a decline in the electrochemical active surface area,[13] lower homogeneity of the catalyst layer,[14] reduced electron transport channels,[13,15] and decreased water transportation.[16]

So far, several strategies are adopted to reduce the anode catalyst loading for PEMWE. Considering the excellent OER performance of Ir- and Ru-based catalysts, many researchers have been devoted to designing novel Ir/Ru-based nanostructured catalysts,[17] such as supported catalysts[18–20] and core–shell structured catalysts.[21–23]

However, a few works focus on the new structure design and preparation techniques of the catalyst layer. Hegge *et al.*[24] utilized electrospinning technology to fabricate high-conductivity IrO_x nanofibers, improving electron conductivity in the catalyst layer. Dong *et al.*[25] proposed a design that

[a]*Institute of Fuel Cells, School of Mechanical Engineering, Shanghai Jiao Tong University, 800 Dongchuan Rd, Shanghai 200240, P. R. China. E-mail: kechangchun@sjtu.edu.cn*

[b]*Foshan Xianhu Laboratory of the Advanced Energy Science and Technology Guangdong Laboratory, Xianhu Hydrogen Valley, Foshan, 528200, P. R. China. E-mail: liguangfu@xhlab.cn*

[c]*School of Chemistry and Chemical Engineering, Shanghai Jiao Tong University, 800 Dongchuan Rd, Shanghai 200240, P. R. China*

enhances mass transport and the three-phase interface in the catalyst layer by utilizing a gradient conical array in the anode catalyst layer. Lu *et al.*[26] synthesized vertically arranged IrO_x nanoarrays utilizing titanium nano-templates as substrates through electrodeposition technology, improving the ion transport capability. However, the complex preparation procedures involved in these methods may pose challenges for practical application.

Although non-noble metals, such as SnO_2, have been studied to reduce the use of Ir, the research has mainly focused on the catalyst level but not on the catalyst layer structure at the electrode level. In this paper, we studied the electrode level strategy for reducing Ir loading by the optimization of the microstructure of the catalyst layer *via* SnO_2 doping. It is found that, under appropriate conditions, the pore structure and electron conductive network of the anode catalyst layer can be simultaneously improved by SnO_2 doping, thus reducing the mass transfer polarization and ohmic polarization. Furthermore, the improved pore structure and enhanced electron conduction network collectively work to minimize the occurrence of charge transfer polarization. As a result, these contribute to a reduction in charge transfer polarization. This paper provides a perspective at the electrode level to reduce the precious metal loading of the anode for PEMWE.

2. Experimental

2.1 Materials

Nation 115 membrane (DuPont), isopropanol (AR, Sinopharm Chemical Reagent), 30 wt% H_2O_2 (AR, Sinopharm Chemical Reagent), 98 wt% H_2SO_4 (AR, Sinopharm Chemical Reagent), Ir black (10 nm, ZKJY), SnO_2 (<50 nm, Aladdin), 70 wt% Pt/C (TANAKA), 5 wt% Nation solution (DuPont), carbon paper (T60), and titanium felt (ZJXY) are used as received.

2.2 The fabrication of membrane electrode assemblies (MEAs)

Firstly, the Nafion 115 membrane was pre-treated by 5 wt% H_2O_2 solution (1 h, 80 °C) and 1 M H_2SO_4 solution (1 h, 80 °C), respectively, as the ref. 27. Before using, the membrane was dried in a vacuum oven for 4 hours at 60 °C.

The anode catalyst ink was formulated by blending iridium black, a certain proportion of SnO_2, 5 wt% Nafion solution, deionized water, and isopropanol. The cathode catalyst ink was formulated by blending Pt/C, 5 wt% Nafion solution, deionized water, and isopropanol. The ionomer content of anode and cathode accounted for 16 wt% and 23 wt%, respectively. The ball milling technique was employed to ensure uniformity of the ink. The anode and cathode ink were sprayed onto the Nafion 115 membrane and carbon paper, respectively. The anode is catalyst coated membrane (CCM), and the cathode is gas diffusion electrode (GDE).

The study involved five sets of CCMs samples, namely CCM-1.5Ir, CCM-2.0Ir, CCM-1.5Ir-0.25SnO_2, CCM-1.5Ir-0.50SnO_2, and CCM-1.5Ir-0.75SnO_2, shown in Table 1.

Table 1 CCM with different anode catalyst layers

Sample	Anode catalyst layer
CCM-1.5Ir	Ir (1.5 mg cm^{-2})
CCM-2.0Ir	Ir (2.0 mg cm^{-2})
CCM-1.5Ir-0.25SnO_2	Ir (1.5 mg cm^{-2}) + SnO_2 (0.25 mg cm^{-2})
CCM-1.5Ir-0.50SnO_2	Ir (1.5 mg cm^{-2}) + SnO_2 (0.50 mg cm^{-2})
CCM-1.5Ir-0.75SnO_2	Ir (1.5 mg cm^{-2}) + SnO_2 (0.75 mg cm^{-2})

2.3 Physical characterizations

The surface morphology of the CCMs were examined using scanning electron microscopy (SEM, VEGA 3). During the imaging process, the secondary electrons were accelerated using a voltage of 20 kV.

Mercury intrusion porosimetry (MIP, MicroActive AutoPore V 9600 2.03.00) was utilized to assess the pore size distribution and porosity of the CCMs. The test pressure range was from 0.5 to 32 990 psia.

2.4 Electrolysis cell test

In the electrolysis cell (as shown in Fig. 1), titanium plates equipped with flow fields were utilized as the end-plates. Polytetrafluoroethylene (PTFE) sealing gaskets were employed for the cathode and anode. Deionized water at 80 °C was circulated through the anode.

The electrochemical tests were conducted using the Gamry Interface 5000E system.

Polarization curve measurement was taken at different current densities. The current density increased by 10 mA cm^{-2} from 10 mA cm^{-2} to 100 mA cm^{-2}, and by 100 mA cm^{-2} from 100 mA cm^{-2} to 1800 mA cm^{-2}.

Electrochemical impedance spectroscopy (EIS) was performed on the electrolysis cell at a current density of 0.1 A cm^{-2}. The amplitude of AC voltage disturbance was 10 mV rms. The frequency range spanned from 10 000 Hz down to 0.2 Hz.

Cyclic voltammetry (CV) was performed on the electrolysis cell at a scanning speed of 50 mV s^{-1}, the voltage range for scanning was set from 0 to 1.2 V.[28] The working electrode (green) and working sense electrode (blue) were connected to the anode of the electrolysis cell, while the reference electrode (white) and counter electrode (red) were connected to the cathode.

The number of voltammetric charge in the electrolysis cell was calculated based on eqn (1).[28]

$$Q = \int_{E_1}^{E_2} \frac{|i|}{\nu} \mathrm{d}E \quad (1)$$

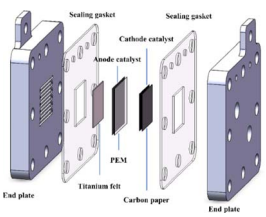

Fig. 1 Schematic diagram of the PEMWE single cell.

where "Q" represents the number of voltammetric charge, "E_1" and "E_2" represent the lowest and highest potentials, respectively, "i" represents the current density, and "ν" is the scanning speed.

2.5 Polarization distribution test and analysis

The whole polarization loss within the electrolysis cell can be calculated using eqn (2).[29]

$$E = E_{\mathrm{rev}} + \eta_{\mathrm{ohm}} + \eta_{\mathrm{ct}} + \eta_{\mathrm{mt}} \quad (2)$$

where "E" represents cell voltage, "E_{rev}" represents reversible cell voltage, "η_{ohm}" represents ohmic polarization, "η_{ct}" represents charge transfer polarization, and "η_{mt}" represents mass transfer polarization. The value of "E_{rev}" is 1.168 V under the given conditions of 80 °C and 1 atmospheric pressure.[29]

The ohmic polarization (ηohm) can be determined using eqn (3).

$$\eta_{\mathrm{ohm}} = j \times R_{\mathrm{ohm}} \quad (3)$$

where "j" represents current density and "R_{ohm}" represents ohmic resistance.

The Tafel slope of the electrolysis cell is analyzed based on the polarization curve.[29] The charge transfer polarization (η_{ct}) can be calculated using eqn (4)–(6).

$$\eta_{\mathrm{ct}} = b \times \log\left(\frac{j}{j_0}\right) \quad (4)$$

$$a = -b \times \log j_0 \quad (5)$$

$$\eta_{\mathrm{ct}} = a + b \times \log j \quad (6)$$

where "j" represents current density, "j_0" represents the exchange current density, "b" represents the Tafel slope, and "a" represents the intercept. The current density (j) is located in the range of 10 mA cm^{-2}–100 mA cm^{-2}.

After subtracting E_{rev}, η_{ohm}, and η_{ct} from the cell voltage (E), the remaining voltage represents the polarization loss of η_{mt} as determined by the eqn (2).

3. Results and discussions

3.1 Polarization distribution analysis of the common Ir based CCM

Analyzing the polarization distribution of various parts (η_{mt}, η_{ohm} and η_{ct}) of common Ir based CCM is beneficial for understanding the problem of low anode noble metal loading at the electrode level, and thus helping us find directions to reduce catalyst loading. The polarization distribution is derived from the Tafel slope and EIS. According to Fig. 2(A), intercept (a) is 0.414 V, Tafel slope (b) is 73.67 mV dec^{-1}, η_{ct} at different current densities can be calculated using eqn (6).[29] According to Fig. 2(B), the ohmic resistance (R_{ohm}) is 0.161 Ω cm^2. Using eqn (3), η_{ohm} is determined.

Fig. 2(C) and (D) show the polarization distribution of the common Ir based CCM (CCM-1.5Ir) at different current densities. It reveals that, for the common Ir based CCM, as the current density increases, the mass transfer polarization increases rapidly, the ohmic polarization increases linearly, while the charge transfer polarization changes slowly. At 1 A cm^{-2}, the ratio of the mass transfer polarization and ohmic polarization are 4.99% and 26.56%, respectively. When the current density reaches 1.8 A cm^{-2}, the ratio of the mass transfer polarization and ohmic polarization reach 16.73% and 33.34%, respectively. It is believed that with the development of PEMWE, the current density would reach a much higher value than 1.8 A cm^{-2}, which would lead to a much higher ratio of mass transfer polarization and ohmic polarization. Therefore, reducing mass transfer polarization and ohmic polarization are crucial in electrode preparation.

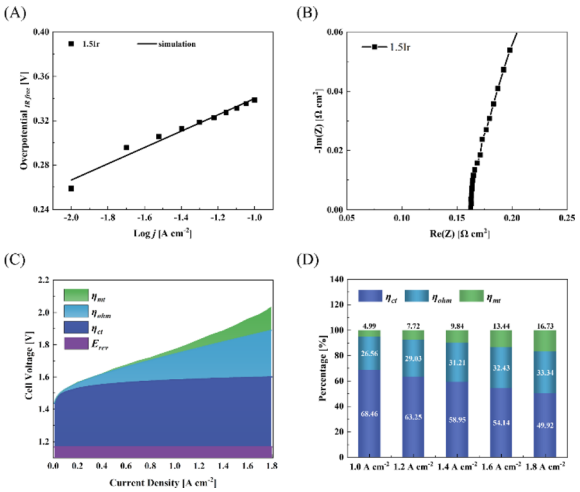

Fig. 2 (A) Tafel fitting slope, (B) electrochemical impedance spectroscopy, (C) polarization distribution and (D) polarization ratio, of CCM-1.5Ir in the PEMWE single cell.

Herein, we propose a simple method, which can synchronously improve the pore structure and electron conductive network of the anode catalyst layer *via* SnO_2 doping, which can effectively reduce the mass transfer polarization, ohmic polarization of the single cell. Interestingly, when the micro-structure of the anode catalyst layer is improved, the charge transfer polarization is also reduced.

3.2 The effect of SnO_2 doping in the micro-structure of the catalyst layer

Fig. 3 depicts the SEM surface images of CCMs. Notably, the catalyst layer of CCM-1.5Ir exhibits relatively narrow and thin ridges on its surface, leading to the lowest surface smoothness among the five samples, as illustrated in Fig. 3(A). This reduces the contact area between the catalyst layer and the proton exchange membrane. In Fig. 3(B), with increasing loading (CCM-2.0Ir), the narrow and thin ridges within the catalyst layer become thicker, while the transition between ridges and pores becomes smoother. Consequently, the contact with the proton exchange membrane improves. Furthermore, upon doping with SnO_2, compared to CCM-1.5Ir, the contact area increases in CCM-1.5Ir-0.25SnO_2 (Fig. 3(C)). However, some of the pores on

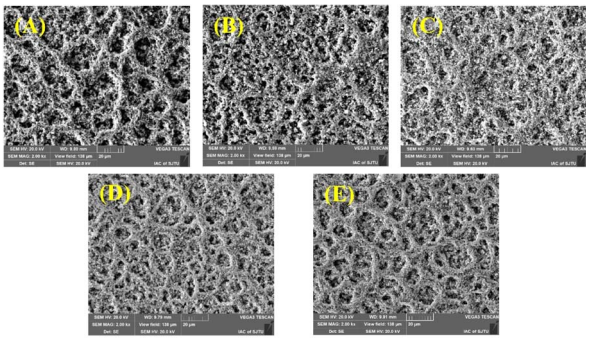

Fig. 3 SEM images of (A) CCM-1.5Ir, (B) CCM-2.0Ir, (C) CCM-1.5Ir-0.25SnO_2, (D) CCM-1.5Ir-0.50SnO_2 and (E) CCM-1.5Ir-0.75SnO_2.

the surface of the catalyst layer are covered, leading to a decrease in the uniform distribution of the pores. Among the five samples, the morphology of CCM-1.5Ir-0.50SnO_2 and CCM-1.5Ir-0.75SnO_2 is most similar (Fig. 3(D) and (E)). However, CCM-1.5Ir-0.75SnO_2 exhibits excessively high ridges, along with some large pores on its catalyst layer surface. In contrast, the surface pore distribution of CCM-1.5Ir-0.50SnO_2 and CCM-2.0Ir is more akin, and the area of the ridges is also more similar among the five samples.

Fig. 4(A) shows the effect of SnO_2 doping on the porosity of the CCM. It suggests that SnO_2 doping could significantly change the porosity and the pore size distributions of the CCM. It is observed, for Ir based CCM, the higher Ir loading of CCM-2.0Ir obtains lower porosity is 8.02%, while the porosity of CCM-1.5Ir is 15.17%. The low porosity of CCM-2.0Ir could result in a reduced specific surface area in the catalyst layer, making it challenging for the active sites to efficiently interact with the reactants, thus hindering the effective participation of certain catalytic active sites in the reaction process. Appropriate content of SnO_2 is beneficial to improving of the porosity of the CCM, the porosity of CCM-1.5Ir-0.25SnO_2 is 18.34%, and the porosity of CCM-1.5Ir-0.50SnO_2 is 18.40%, both higher than CCM-1.5Ir. Higher content of SnO_2 may make the original pores blocked, resulting in a higher number of dead pores within the catalyst layer.

The pore size distributions of the CCMs can also be altered by the SnO_2 doping (Fig. 4(B)). For example, the pore size distribution of CCM-1.5Ir is mainly below 25 nm, while the pore size distribution of CCM-1.5Ir-0.50SnO_2 is mainly between 10–40 nm.

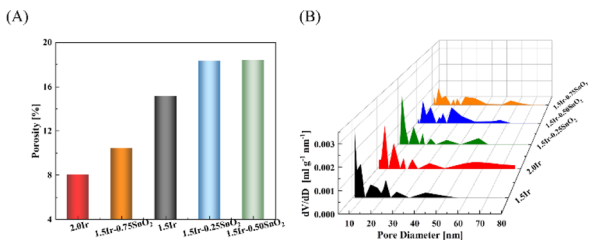

Fig. 4 (A) Porosity and (B) pore size distribution measured by MIP of CCM with different anode catalyst layers.

CCM-1.5Ir-0.50SnO_2 and CCM-1.5Ir-0.25SnO_2 have similar porosity, with values of 18.40% and 18.34% respectively, but their pore size distributions are different. CCM-1.5Ir-0.50SnO_2 has a larger pore size distribution. CCM-1.5Ir-0.50SnO_2 and CCM-1.5Ir-0.75SnO_2 have similar pore size distributions (10–40 nm), but their porosity values are different. CCM-1.5Ir-0.75SnO_2 has a porosity of only 10.44%.

3.3 Electrochemical performance of different CCMs

It can be observed from Fig. 5(A), at 1 A cm^{-2}, the cell voltages of CCM-1.5Ir, CCM-2.0Ir and CCM-1.5Ir-0.50SnO_2 are 1.772 V, 1.703 V and 1.706 V respectively. The performance of CCM-1.5Ir-0.50SnO_2 surpasses CCM-1.5Ir, and is close to that of CCM-2.0Ir, in spite of lower Ir loading. Fig. 5(B) shows the single cell performance of the CCM with different content of SnO_2. The cell voltage of CCM-1.5Ir-0.25SnO_2 and CCM-1.5Ir-0.75SnO_2 at a current density of 1 A cm^{-2} is 1.723 V and 1.756 V, respectively, and it was observed that CCM-1.5Ir-0.50SnO_2 exhibits the best performance.

Fig. 6 and Table 2 show the ohmic resistance of the single cell with different CCMs. The CCM-1.5Ir demonstrates high ohmic resistance, which is 0.161 Ω cm^2. As the catalyst loading increases, the ohmic resistance decreases. The CCM-2.0Ir sample exhibits an ohmic resistance of 0.146 Ω cm^2. According to the morphological analysis, it can be attributed to the fact that CCM-2.0Ir exhibits a better interface contact. And the electron conductive network within CCM-2.0Ir is expected to be superior to that of CCM-1.5Ir. According to Fig. 6(A), it can be observed that when the catalyst loading is low, the electrolysis cell exhibits a high ohmic resistance. This is because as the catalyst loading increases, the catalyst layer has a flatter surface

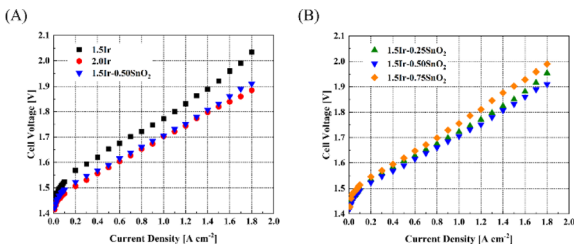

Fig. 5 Polarization curves of the PEMWE single cell. (A) Comparison of with and without SnO_2 doping, and (B) comparison with different quantities of SnO_2 doping.

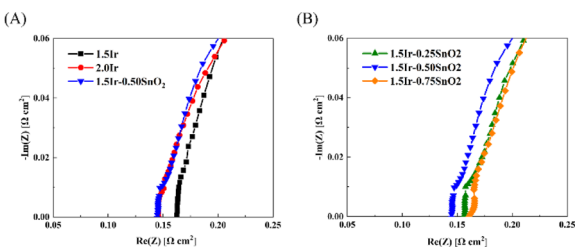

Fig. 6 EIS of the PEMWE single cell. (A) Comparison of with and without SnO_2 doping, (B) comparison with different content of SnO_2 doping.

Table 2 High frequency resistance of electrolysis cell with different CCM at 0.1 A cm^{-2}

CCM	R_{ohm} (Ω cm^2)
CCM-1.5Ir	0.161
CCM-2.0Ir	0.146
CCM-1.5Ir-0.25SnO_2	0.156
CCM-1.5Ir-0.50SnO_2	0.145
CCM-1.5Ir-0.75SnO_2	0.162

and better conductive electron network. According to Fig. 6(B), when the same catalyst loading is employed, the ohmic resistance of the single cell decreases after the anode is doped with appropriate proportion of SnO_2. Especially, CCM-1.5Ir-0.50SnO_2 exhibits the lowest ohmic resistance of 0.145 Ω cm^2.

However, when the SnO_2 content is too high, the ohmic resistance of the electrolysis cell does not continue to decrease. CCM-1.5Ir-0.75SnO_2 exhibits the highest ohmic resistance of 0.162 Ω cm^2, even exceeding CCM-1.5Ir. SnO_2 exhibits a relatively high electron mobility (240 cm^2 V^{-1} s^{-1}),[30] but as a noble metal, the electron mobility of Ir catalyst is even higher (1370 cm^2 V^{-1} s^{-1}).[31] Consequently, excessive doping of SnO_2 leads to an increase in the ohmic resistance, such as CCM-1.5Ir-0.75SnO_2. However, the lower ohmic resistance of CCM-1.5Ir-0.50SnO_2 is attributed to the optimization of its catalyst layer structure through SnO_2 doping. Excessive doping of SnO_2 leads to the unfavorable changes in the internal structure of the anode catalyst layer. This hinders electron conduction.

According to Fig. 7(A), the Tafel slopes of different samples can be fitted. The Tafel slope of CCM-1.5Ir, CCM-2.0Ir, CCM-1.5Ir-0.25SnO_2, CCM-1.5Ir-0.50SnO_2, and CCM-1.5Ir-0.75SnO_2 are 73.67 mV dec^{-1}, 49.25 mV dec^{-1}, 52.22 mV dec^{-1}, 59.27 mV dec^{-1}, and 65.68 mV dec^{-1}, respectively. CCM-2.0Ir exhibits the lowest Tafel slope due to its highest anode Ir loading. And intercept of Tafel line for MEA-1.5Ir, MEA-2.0Ir, MEA-1.5Ir-0.25SnO_2, MEA-1.5Ir-0.50SnO_2, and MEA-1.5Ir-0.75SnO_2 are 0.414 V, 0.345 V, 0.367 V, 0.369 V, and 0.395 V, respectively. The Tafel slopes and intercept of CCM-1.5Ir-0.25SnO_2, CCM-1.5Ir-0.50SnO_2, and CCM-1.5Ir-0.75SnO_2 are lower than that of CCM-1.5Ir. When SnO_2 is doped, the Tafel slope and intercept decreases. This indicates an improvement in the electrochemical reaction capability of the single cell, which may be related to the voltammetric charge of the electrolysis cell.

The calculation of voltammetric charge originates from Fig. 8(A). As shown in Fig. 8(B), the voltammetric charge of

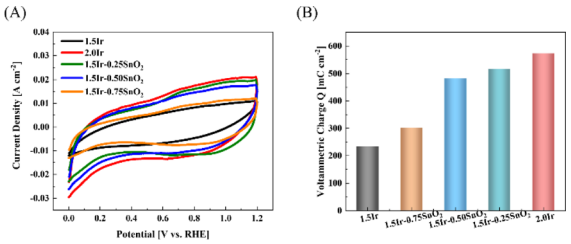

Fig. 8 (A) CV curves, and (B) voltammetric charge Q of the PEMWE single cell of different samples.

CCM-1.5Ir, CCM-2.0Ir, CCM-1.5Ir-0.25SnO_2, CCM-1.5Ir-0.50SnO_2, and CCM-1.5Ir-0.75SnO_2 is 233 mC cm^{-2}, 573 mC cm^{-2}, 516 mC cm^{-2}, 482 mC cm^{-2} and 301 mC cm^{-2}, respectively. It is observed that CCM-2.0Ir has the largest voltammetric charge, due to the higher anode Ir loading in CCM-2.0Ir. The voltammetric charge of CCM-1.5Ir-0.25SnO_2, CCM-1.5Ir-0.50SnO_2, and CCM-1.5Ir-0.75SnO_2 are slightly higher than CCM-1.5Ir, despite of the same anode Ir loading. It suggests that the doping of SnO_2 is beneficial to improving the voltammetric charge of the anode electrode. When the catalyst is not doped with SnO_2, the imperfect micro-structure of the catalyst layer limits the transport of reactants and products. Consequently, some Ir particles are not efficiently functional. Therefore, it has a lower number of voltammetric charge, resulting in a poor electrochemical reaction capability.

Nevertheless, it is observed that the voltammetric charge decreases with increased amount of SnO_2 doping. This suggests that excessive SnO_2 doping may result in the blockage of some Ir catalyst active sites, thereby negatively impacting the electrochemical performance.

Fig. 9(A) and (B) show the polarization distribution at different current densities of CCM-1.5Ir-0.50SnO_2. After doping SnO_2 in the anode catalyst layer, the mass transfer polarization, ohmic polarization and charge transfer polarization of the electrolysis cell were reduced compared to the CCM-1.5Ir. The CCM-1.5Ir-0.50SnO_2 has the largest porosity (18.40%) and a larger pore size distribution (10–40 nm). Therefore, the decrease in mass transfer polarization from 0.143 V to 0.098 V at 1.8 A cm^{-2}. Especially, with the proportion of mass transfer polarization decreasing from 16.73% to 13.78% at 1.8 A cm^{-2} is most significant. This indicates that the doping of SnO_2 has a positive effect on suppressing mass transfer polarization,

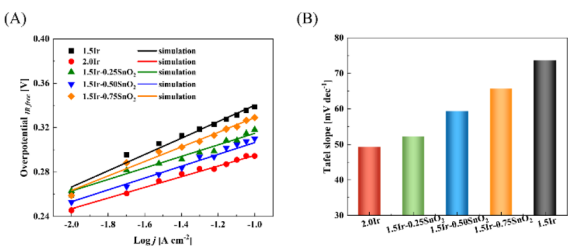

Fig. 7 (A) Tafel fitting and (B) Tafel slope histogram of the PEMWE single cell of five samples.

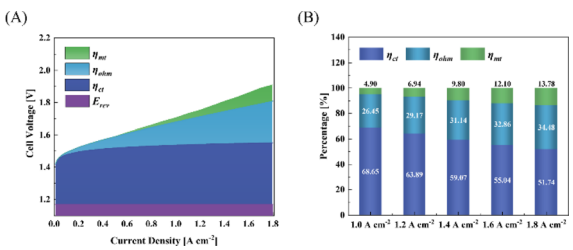

Fig. 9 (A) Polarization distribution, (B) polarization ratio under different current densities of CCM-1.5Ir-0.50SnO_2.

since the doping of SnO_2 improving the pore structure of the CCM. Due to the flatness of the interface and the improvement of electron conduction pathways in the catalyst layer, it decreased ohmic polarization from 0.291 V to 0.260 V at 1.8 A cm^{-2}. Moreover, its charge transfer polarization has decreased from 0.433 V to 0.384 V at 1.8 A cm^{-2}, due to the structure improved in the catalyst layer. This structure facilitates the access of reactants to the catalytic active sites and the release of products from the catalytic active sites.

4. Conclusions

This paper focuses on the electrode level strategy for reducing Ir loading by the optimization of the micro-structure of the catalyst layer *via* SnO_2 doping. It is found, SnO_2 doping could effectively change the micro-structure of the anode catalyst layer. Under appropriate conditions, the pore structure and electron conductive network of the anode catalyst layer could be synchronously improved by SnO_2 doping, thus reduce the mass transfer polarization and ohmic polarization of the anode catalyst layer. Furthermore, the combination of an improved pore structure and an enhanced electron conduction network collaboratively contributes to the reduction of charge transfer polarization. Consequently, these factors contribute to a decrease in charge transfer polarization. This strategy reveals that CCM-1.5Ir-0.50SnO_2 exhibits superior electrochemical performance compared to CCM-1.5Ir, as observed from the polarization curve. Additionally, the performance of CCM-1.5Ir-0.50SnO_2 at a loading of only 1.5 mg cm^{-2} is similar to the CCM-2.0Ir with a loading of 2.0 mg cm^{-2}, which means that SnO_2 doping saves about 25% loading of Ir. This paper provides a perspective and understanding at the electrode level to reduce the precious metal loading of the anode in PEMWE.

Conflicts of interest

The authors declare no conflict of interest.

Acknowledgements

Thanks to Key-area R&D Programme of Guangdong Province, China (2021B0707040001). National Natural Science Foundation of China (Project number: 21406220) for supporting this research.

Notes and references

1 Z. Kang, J. Mo, G. Yang, S. T. Retterer, D. A. Cullen, T. J. Toops, J. B. Green Jr, M. M. Mench and F.-Y. Zhang, *Energy Environ. Sci.*, 2017, **10**, 166–175.
2 Z. Kang, T. Schuler, Y. Chen, M. Wang, F.-Y. Zhang and G. Bender, *Electrochim. Acta*, 2022, **429**, 140942.
3 J. O. Majasan, J. I. S. Cho, I. Dedigama, D. Tsaoulidis, P. Shearing and D. J. L. Brett, *Int. J. Hydrogen Energy*, 2018, **43**, 15659–15672.
4 R.-T. Liu, Z.-L. Xu, F.-M. Li, F.-Y. Chen, J.-Y. Yu, Y. Yan, Y. Chen and B. Y. Xia, *Chem. Soc. Rev.*, 2023, **52**, 5652–5683.
5 Z. Kang, M. Pak and G. Bender, *Int. J. Hydrogen Energy*, 2021, **46**, 15161–15167.
6 N. Yoshinaga, Y. Kanai, T. Fukazawa, Y. Nakano and W. Mei, *ECS Meeting Abstracts*, 2019, vol. MA2019-02, pp. 1712–1712.
7 C. Spori, L. J. Falling, M. Kroschel, C. Brand, A. Bonakdarpour, S. Kuhl, D. Berger, M. Gliech, T. E. Jones, D. P. Wilkinson and P. Strasser, *ACS Appl. Mater. Interfaces*, 2021, **13**, 3748–3761.
8 K. Ayers, N. Danilovic, R. Ouimet, M. Carmo, B. Pivovar and M. Bornstein, *Annu. Rev. Chem. Biomol. Eng.*, 2019, **10**, 219–239.
9 T. L. Doan, H. E. Lee, M. Kim, W. C. Cho, H. S. Cho and T. Kim, *J. Power Sources*, 2022, **533**, 231370.
10 C. J. Lee, J. Song, K. S. Yoon, Y. Rho, D. M. Yu, K.-H. Oh, J. Y. Lee, T.-H. Kim, Y. T. Hong, H.-J. Kim, S. J. Yoon and S. So, *J. Power Sources*, 2022, **518**, 230772.
11 C. Liu, M. Shviro, A. S. Gago, S. F. Zaccarine, G. Bender, P. Gazdzicki, T. Morawietz, I. Biswas, M. Rasinski, A. Everwand, R. Schierholz, J. Pfeilsticker, M. Müller, P. P. Lopes, R.-A. Eichel, B. Pivovar, S. Pylypenko, K. A. Friedrich, W. Lehnert and M. Carmo, *Adv. Energy Mater.*, 2021, **11**, 2002926.
12 A. S. Pushkarev, I. V. Pushkareva, M. A. Solovyev, M. Prokop, T. Bystron, S. K. Rajagopalan, K. Bouzek and S. A. Grigoriev, *Electrochim. Acta*, 2021, **399**, 139436.
13 C. Rozain, E. Mayousse, N. Guillet and P. Millet, *Appl. Catal., B*, 2016, **182**, 153–160.
14 M. Bernt, A. Siebel and H. A. Gasteiger, *J. Electrochem. Soc.*, 2018, **165**, F305–F314.
15 Q. Feng, X. Z. Yuan, G. Liu, B. Wei, Z. Zhang, H. Li and H. Wang, *J. Power Sources*, 2017, **366**, 33–55.
16 J. Lopata, Z. Kang, J. Young, G. Bender, J. W. Weidner and S. Shimpalee, *J. Electrochem. Soc.*, 2020, **167**(6), 064507.
17 Y. Chen, C. Liu, J. Xu, C. Xia, P. Wang, B. Y. Xia, Y. Yan and X. Wang, *Small Struct.*, 2022, **4**, 2200130.
18 M. Möckl, M. F. Ernst, M. Kornherr, F. Allebrod, M. Bernt, J. Byrknes, C. Eickes, C. Gebauer, A. Moskovtseva and H. A. Gasteiger, *J. Electrochem. Soc.*, 2022, **169**, 064505.
19 V. K. Puthiyapura, M. Mamlouk, S. Pasupathi, B. G. Pollet and K. Scott, *J. Power Sources*, 2014, **269**, 451–460.
20 W. Sun, Z. Wang, X. Tian, H. Deng, J. Liao, C. Ma, J. Yang, X. Gong, W. Huang and C. Ge, *Nanoscale*, 2021, **13**, 13845–13857.
21 J. Shan, C. Guo, Y. Zhu, S. Chen, L. Song, M. Jaroniec, Y. Zheng and S.-Z. Qiao, *Chem*, 2019, **5**, 445–459.
22 C. V. Pham, M. Bühler, J. Knöppel, M. Bierling, D. Seeberger, D. Escalera-López, K. J. J. Mayrhofer, S. Cherevko and S. Thiele, *Appl. Catal., B*, 2020, **269**, 118762.
23 H. N. Nong, T. Reier, H.-S. Oh, M. Gliech, P. Paciok, T. H. T. Vu, D. Teschner, M. Heggen, V. Petkov, R. Schlögl, T. Jones and P. Strasser, *Nat. Catal.*, 2018, **1**, 841–851.
24 F. Hegge, F. Lombeck, E. Cruz Ortiz, L. Bohn, M. von Holst, M. Kroschel, J. Hübner, M. Breitwieser, P. Strasser and S. Vierrath, *ACS Appl. Energy Mater.*, 2020, **3**, 8276–8284.
25 S. Dong, C. Zhang, Z. Yue, F. Zhang, H. Zhao, Q. Cheng, G. Wang, J. Xu, C. Chen, Z. Zou, Z. Dou and H. Yang, *Nano Lett.*, 2022, **22**, 9434–9440.

26 Z.-X. Lu, Y. Shi, P. Gupta, X.-p. Min, H.-y. Tan, Z.-D. Wang, C.-q. Guo, Z.-q. Zou, H. Yang, S. Mukerjee and C.-F. Yan, *Electrochim. Acta*, 2020, **348**, 136302.
27 H. Lv, G. Zhang, C. Hao, C. Mi, W. Zhou, D. Yang, B. Li and C. Zhang, *RSC Adv.*, 2017, **7**, 40427–40436.
28 G. Jiang, H. Yu, J. Hao, J. Chi, Z. Fan, D. Yao, B. Qin and Z. Shao, *J. Energy Chem.*, 2019, **39**, 23–28.
29 H. Lv, S. Wang, Y. Sun, J. Chen, W. Zhou and C. Zhang, *J. Power Sources*, 2023, **564**, 232878.
30 Y. Zhao, L. Gao, Q. Wang, Q. Zhang, X. Yang, J. Zhu, H. Huang, J. Duan and Q. Tang, *Carbon Energy*, 2024, e468.
31 M. A. Basyooni, M. Tihtih, I. Boukhoubza, J. E. F. M. Ibrahim, R. En-nadir, A. M. Abdelbar, K. Rahmani, S. E. Zaki, Ş. Ateş and Y. R. Eker, *Phys. Status Solidi RRL*, 2023, **18**, 2300257.